

Article

CO₂ Adsorption by Amino-Functionalized Graphene–Silica Gels

Marina González-Barriuso ^{1,*} , Ángel Yedra ² and Carmen Blanco ¹

¹ Materials Chemistry Group, Department QulPRE, Universidad de Cantabria, Av. de los Castros 46, 39005 Santander, Spain; carmen.banco@unican.es

² Fundación Centro Tecnológico de Componentes, C/Isabel Torres 1, 39011 Santander, Spain; ayedra@centrotecnologicocctc.com

* Correspondence: marina.gonzalez@unican.es

Abstract

This work evaluates the CO₂-adsorption relevance and cycling stability of graphene oxide–silica (GO–SiO₂) and reduced graphene oxide–silica (rGO–SiO₂) gels after amine functionalization, demonstrating high-capacity retention under repeated adsorption–desorption cycles: rGO–SiO₂–APTMS retains ≈96.3% of its initial uptake after 50 cycles, while GO–SiO₂–APTMS retains ≈90.0%. The use of surfactants to control the organization of inorganic and organic molecules has enabled the development of ordered mesostructures, such as mesoporous silica and organic/inorganic nanocomposites. Owing to the outstanding properties of graphene and its derivatives, synthesizing mesostructures intercalated between graphene sheets offers nanocomposites with novel morphologies and enhanced functionalities. In this study, GO–SiO₂ and rGO–SiO₂ gels were synthesized and characterized by X-ray diffraction (XRD), differential scanning calorimetry (DSC), thermogravimetric analysis (TG), mass spectrometry (MS), N₂ adsorption–desorption isotherms, and transmission electron microscopy (TEM). The resulting materials exhibit a laminar architecture, with mesoporous silica domains grown between graphene-based layers; the silica contents are 83.6% and 87.6%, and the specific surface areas reach 446 and 710 m²·g^{−1}, respectively. The laminar architecture is retained regardless of the surfactant-removal route; however, in GO–SiO₂ obtained by solvent extraction, a fraction of the surfactant remains partially trapped. Together with their high surface area, hierarchical porosity, and amenability to surface functionalization, these features establish amine-grafted graphene–silica gels, particularly rGO–SiO₂–APTMS, as promising CO₂-capture adsorbents.

Keywords: graphene; graphene oxide; mesostructure; silica gels; sol–gel; amine functionalization; surfactant removal; CO₂ capture



Academic Editor: Duckjong Kim

Received: 5 August 2025

Revised: 26 August 2025

Accepted: 1 September 2025

Published: 2 September 2025

Citation: González-Barriuso, M.; Yedra, Á.; Blanco, C. CO₂ Adsorption by Amino-Functionalized Graphene–Silica Gels. *Gels* **2025**, *11*, 702. <https://doi.org/10.3390/gels11090702>

Copyright: © 2025 by the authors. Licensee MDPI, Basel, Switzerland. This article is an open access article distributed under the terms and conditions of the Creative Commons Attribution (CC BY) license (<https://creativecommons.org/licenses/by/4.0/>).

1. Introduction

Graphene and its derivatives, such as graphene oxide (GO), reduced graphene oxide (rGO), and graphene nano-platelets, exhibit properties that make them suitable for numerous applications [1,2]. Table 1 presents a summary of these applications with examples. Combining these properties with ordered mesostructures gives rise to a new kind of composite [3–9]. Ordered mesostructures are commonly synthesized using surfactants as templates to direct structural organization.

Table 1. Representative applications of graphene and its derivatives.

Application	Material	Reference
Batteries	Titanium dioxide (TiO ₂)–graphene aerogel composites	[6]
	Laser-induced graphene	[10]
	Graphene nanosheets–Li ₂ S composites	[11]
	Fluorinated graphene oxide	[12]
	ZrN@reduced graphene oxide composite	[13]
Supercapacitors	Sulfonate graphene–N-doped mesoporous carbon composites	[7]
	GO/ZnO	[14]
	Fe ₂ O ₃ /rGO	[15]
	MXene–graphene oxide composite	[16]
Water purification	Mesoporous graphene oxide–SBA-15 nanocomposites	[8]
	GO–CNT–AgI nanocomposite	[17]
	Anthraquinone-2-carboxylic acid on aminated graphene sheets	[18]
	Graphene oxide membrane	[19]
CO ₂ adsorption	Amine-modified silica–reduced graphene oxide composites	[9]
	Modified graphene	[20]

Composites that couple graphene derivatives with ordered mesostructures have been explored for different applications depending on their composition and final structure. For example, titanium dioxide (TiO₂)–graphene aerogel composites are synthesized as anode materials for lithium-ion batteries [6]. TiO₂ is an abundant Li-ion insertion material that undergoes less than ~4% volume expansion during cycling, making it attractive as an anode. However, TiO₂ polymorphs possess relatively low theoretical capacity, electronic conductivity, and Li-ion diffusion coefficients. Incorporation of graphene into TiO₂ mesostructures mitigates these drawbacks. Sulfonate graphene–N-doped mesoporous carbons composites have been used for supercapacitor applications [7]. Graphene is a promising supercapacitor–electrode material owing to its high electrical conductivity, large specific surface area, and chemical stability, while ordered mesoporous silica provide well-controlled porosity and a large surface area; their combination prevents graphene sheet agglomeration and leverages the advantages of both materials. Furthermore, mesoporous graphene oxide/SBA-15 nanocomposites have been developed for water purification [8]. GO is an effective adsorbent for removing organic and inorganic species from water; however, its hydrophilicity and the difficulty in filtration and reuse limit practical application, necessitating a support such as SBA-15. Another application of graphene structures is CO₂ adsorption: amine-modified silica–reduced graphene oxide composites have been investigated for this purpose [9], where graphene derivatives are incorporated into a silica framework to improve thermal stability.

Herein, graphene oxide–silica (GO–SiO₂) and reduced graphene oxide–silica (rGO–SiO₂) gels are prepared by the sol–gel method. Once functionalized with amine groups, these materials are intended for CO₂ capture. For such processes, both silica-based and carbonaceous materials have been studied [20–23]. Combining them into graphene–silica gels is expected to improve CO₂ capture performance. In this study, silica was intercalated between the laminar structure of GO. The mesoporous silica was confined between the adjacent flat surfaces of the GO, reinforcing its mesostructure. For instance, these mesostructures are used for environmental remediation applications. This confinement between

the sheets allowed the mesoporous silica to intercalate compactly between two sheets of these carbon structures, developing mesoporous material in the galleries of both graphene derivatives. The synthesized samples were characterized, and their results were compared.

Removal of the surfactant used to template these materials is a critical step because improper removal compromises textural parameters. This is particularly important if the chemical characteristics of the GO (notably, the hydroxide and acid groups) must be preserved. For GO-SiO₂, the surfactant was removed by solvent extraction [24,25], whereas for rGO-SiO₂ it was eliminated by calcination [26–28]. These calcination processes achieved a reduction in GO and surfactant elimination in a single step.

2. Results and Discussion

2.1. Characterization of rGO-SiO₂ and GO-SiO₂ Gels

XRD was used to examine whether the basal spacing between the GO sheets changes upon intercalation of the template (CTAB). Figure 1 shows the XRD patterns for GO and GO-CTAB. The presence of diffraction peaks confirms the laminar structure of both samples. After the CTAB intercalation, the basal spacing increases. According to Bragg's law, the GO-CTAB sample exhibits a basal spacing of 33 Å prior to subsequent hydrolysis with either silica source, whereas pristine GO shows 10 Å.

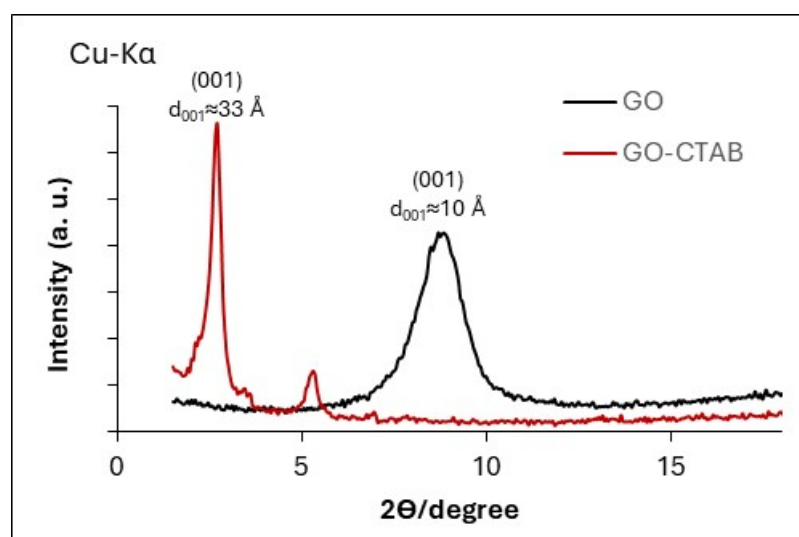


Figure 1. XRD patterns of GO (graphene oxide) and GO-CTAB (graphene oxide treated with CTAB). The basal reflection is indexed as (001); d_{001} increases from ~ 10 Å (GO, $2\theta \approx 8.8^\circ$, Cu K α) to ~ 33 Å (GO-CTAB, $2\theta \approx 2.7^\circ$) upon CTAB intercalation, evidencing gallery expansion.

Figure 2 shows the deconvolution of the high-resolution C 1s XPS spectra of the GO-SiO₂ and rGO-SiO₂ samples. The chemical state and functional groups can be evaluated from these spectra. The deconvoluted C 1s components are assigned to C-C/C=C bonds (284.0 and 284.4 eV), C-OH (285.3 eV), C-O-C (286.4 and 286.2 eV), C=O (287.6 eV), and O-C=O (288.5/289.0 eV) [29–31]. Each component contributes a given percentage of the total C 1s area, reflecting the fraction of carbon in that functional environment. As expected, GO-SiO₂ contains a higher proportion of oxygenated carbon groups than rGO-SiO₂ (44.2% vs. 22.3%), consistent with the partial reduction in GO during the thermal treatment used to prepare rGO-SiO₂. This thermal treatment was not applied to GO-SiO₂ because CTAB was removed by solvent extraction.

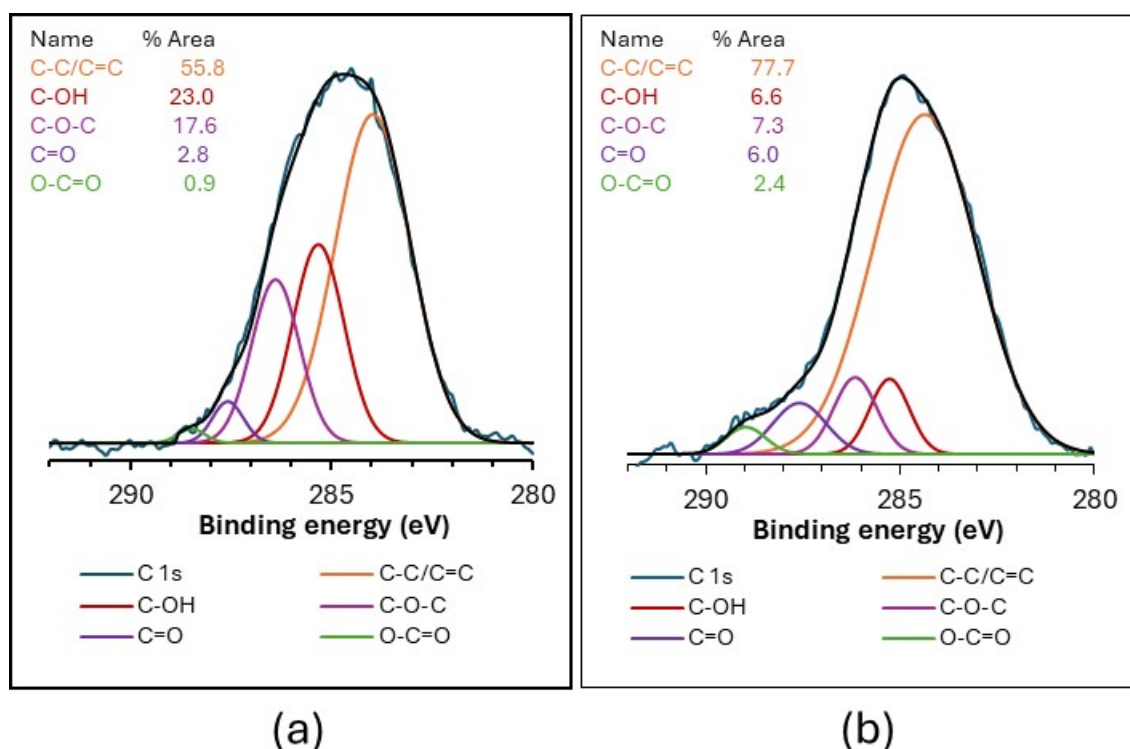


Figure 2. High-resolution C 1s XPS spectra of GO-SiO₂ (graphene oxide–silica gel) (a) and rGO-SiO₂ (reduced graphene oxide–silica gel) (b).

The high-resolution Si 2p XPS spectra of GO-SiO₂ and rGO-SiO₂ show a single component at 103.0 eV attributable to a Si–O bond [31] (Figure 3). Together with the C 1s spectra data, this indicates no detectable covalent interactions between carbons in the graphene structures and silicon in the silica.

The Si 2p region shows no measurable shift between GO-SiO₂ and rGO-SiO₂, with a single Si–O component at 103.0 eV in both samples, indicating an unchanged silica environment and no evidence of Si–C bond formation. In the C 1s region, rGO-SiO₂ exhibits a slight positive shift of the graphitic C–C/C=C component (284.4 eV vs. 284.0 eV in GO-SiO₂), a small negative shift of C–O–C (286.2 eV vs. 286.4 eV), and a modest positive shift of O–C=O (289.0 eV vs. 288.5 eV). These changes ($\Delta BE \approx +0.4$, -0.2 , and $+0.5$ eV, respectively) are consistent with a partial reduction in GO upon calcination (altering the local electronic environment and redistributing oxygenated functionalities), together with minor differential charging expected for these insulating, silica-rich gels. Overall, the spectra reflect a reorganization of surface oxygen groups rather than the emergence of new silicon–carbon bonding.

Figure 4 presents the TG curves of GO and GO-CTAB, which exhibit an initial mass loss of up to 100 °C due to desorption of water, a second mass loss around 220 °C associated with degradation of oxygen-containing surface groups, and a third mass loss near 510 °C due to combustion of the carbon framework. GO-CTAB also shows a mass loss between 200 and 320 °C corresponding to decomposition of the cetyltrimethylammonium bromide surfactant. In both samples, mass loss progresses to completion by 800 °C.

A thermogravimetric analysis of GO-SiO₂ is shown in Figure 5. Five mass loss steps are observed. The first, at around 80 °C, corresponds to the loss of adsorbed water (2.0%) and an endothermic peak. Both features are corroborated by the DSC curve and by monitoring m/z 18 (water) and 44 (carbon dioxide) in the MS; see Figure 5a,b, respectively. Three subsequent steps correspond to exothermic peaks with minima at around 280, 340, and 530 °C. These are assigned to (i) decomposition of oxygenated groups

on GO at 280 °C (2.4%), which appears as a shoulder in the m/z 18 signal (Figure 5b); (ii) decomposition of residual CTAB at 340 °C (3.6%), consistent with concurrent m/z 18 and 44 signals (Figure 5b); and (iii) decomposition of GO at 530 °C (8.4%), again accompanied by H_2O and CO_2 signals (Figure 5b). Finally, an exothermic peak at 640 °C with a CO_2 MS signal is observed, also attributable to carbon decomposition. This peak is more intense in the rGO-SiO₂, likely due to carbonaceous residues after thermal surfactant removal. The solid residue from the GO-SiO₂ analysis is a white powder (83.6%), attributable to the silica content.

Similarly, the rGO-SiO₂ thermogravimetric analysis (Figure 5c,d) shows two mass loss steps. The first, at around 80 °C, corresponds to desorption of water (2.4%) and an endothermic peak, as corroborated by DSC and MS (m/z 18 and 44). The second (10.0%) encompasses two exothermic peaks with minima near 580 °C and a sharper feature at 700 °C, due to the decomposition of the carbonaceous traces associated with rGO. In this sample, 87.6% remains as an inorganic residue, corresponding to silica.

Comparing the GO-SiO₂ and rGO-SiO₂ TG curves indicates that calcination to 380 °C removes CTAB completely from GO-CTAB-SiO₂, whereas solvent extraction leaves residual surfactant within the pore structure. Moreover, solvent extraction preserves the oxygenated groups of GO, while thermal treatment reduces the surface to rGO.

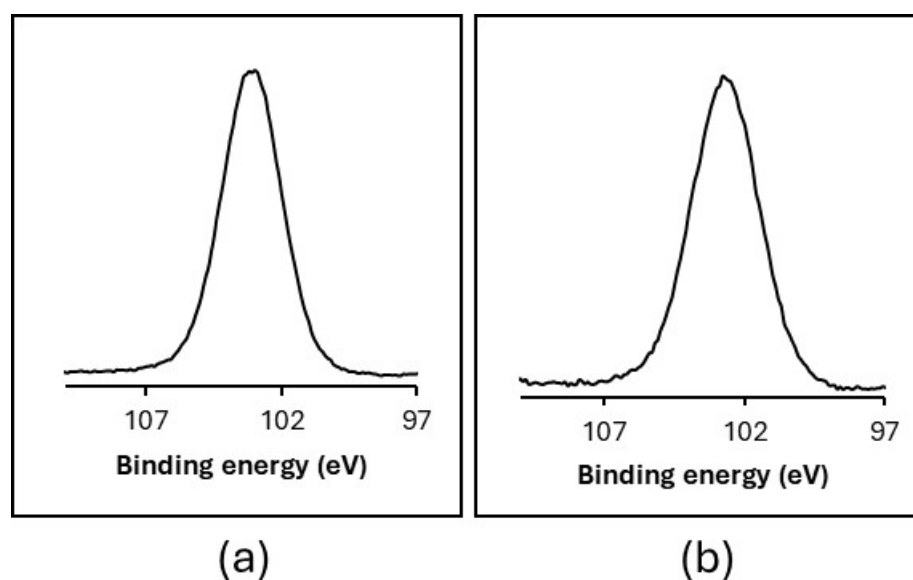


Figure 3. High-resolution Si 2p XPS spectra of GO-SiO₂ (a) and rGO-SiO₂ (b).

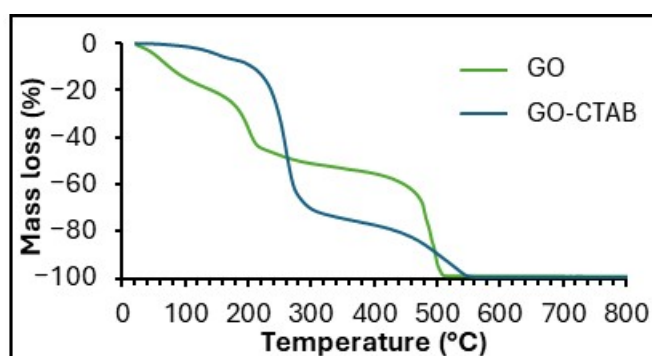


Figure 4. TG curves of GO and GO-CTAB.

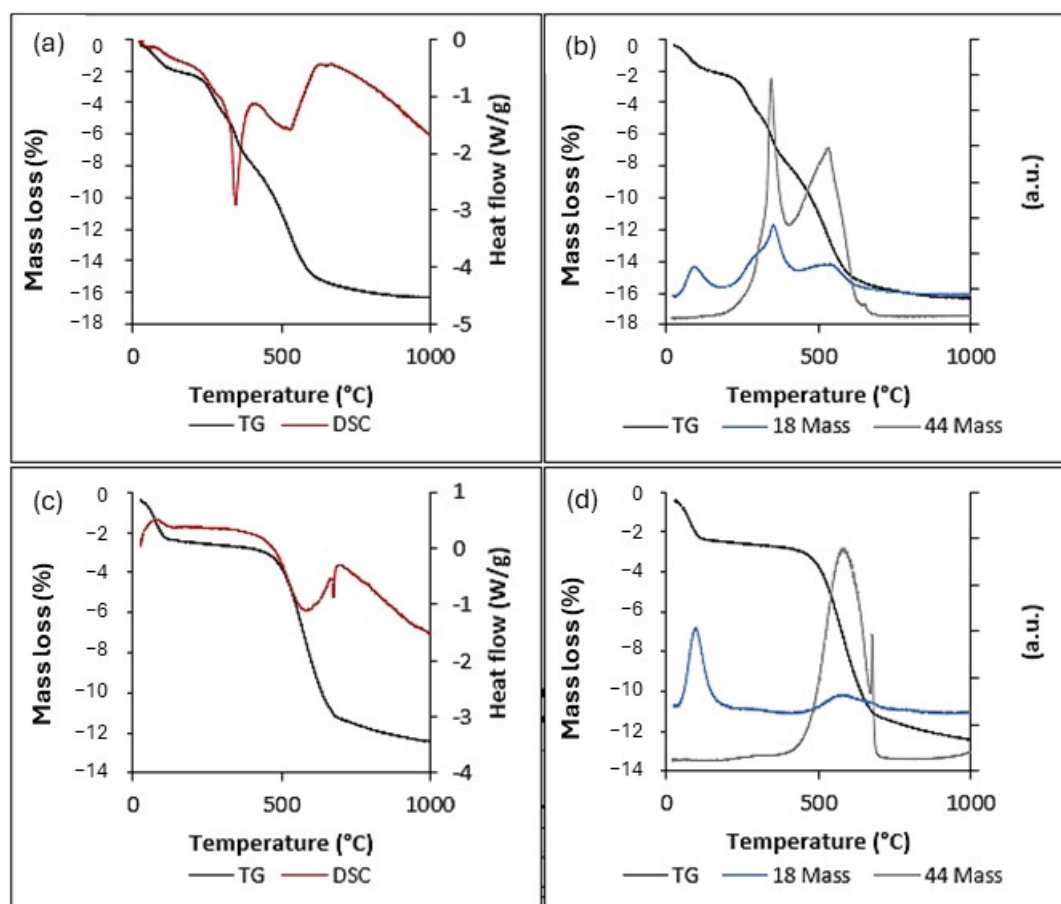


Figure 5. GO-SiO₂ sample: (a) TG (black) and DSC (red); (b) TG (black), with MS monitoring at *m/z* 18 (blue) and 44 (green). rGO-SiO₂ sample: (c) TG (black) and DSC (red); (d) TG (black) with monitoring at *m/z* 18 (blue) and 44 (green).

Figure 6b shows the N₂ adsorption–desorption isotherms and the pore-size distributions of GO-SiO₂ and rGO-SiO₂. Both materials exhibit type IV(a) adsorption isotherms, with an H3 hysteresis loop, characteristic of mesoporous adsorbents with slit-like (laminar) pores, as per the IUPAC classification [32,33]. The nearly linear adsorption between relative pressures of 0.03 and 0.25 is consistent with pores in the 15–30 Å range. The pore distribution obtained by the BJH method (Figure 6a) shows average diameters of 23 Å (GO-SiO₂) and 27 Å (rGO-SiO₂), consistent with slit-like mesopores inferred from the H3 hysteresis; the corresponding modal pore diameters (*D*_{pore}) are reported in Table 2.

The GO-SiO₂ and rGO-SiO₂ gels display type IV(a) isotherms with H3 hysteresis and mesopores around 20–30 Å (Figure 6), with *S*_{BET} = 446 and 710 m² g^{−1} and *V*_{pore} = 0.46 and 0.76 cm³ g^{−1} (Table 2), respectively. These metrics are within or above the ranges commonly reported for amine-grafted mesoporous silicas (where grafting usually lowers *S*_{BET} relative to the parent silica). In contrast, zeolites are predominantly microporous (<1 nm), which can restrict access for bulky organosilanes, while many MOFs offer very high nominal surface areas but largely microporous frameworks and different stability/operability windows.

The specific surface area, average pore size, and N₂ uptake are larger for rGO-SiO₂ than for GO-SiO₂ (Table 2). These differences arise from the amount of surfactant removed by each method, either thermal treatment or solvent extraction. Calcination not only eliminates CTAB but also partially reduces the oxygenated groups on GO, in agreement with the thermogravimetric analysis (Figure 4).

TEM images (Figure 7) show that both gels possess a laminar structure with mesopore silica grown between the GO-based sheets. The sheets are arranged parallel to each other, with regular inter-sheet spacing of around 250 Å for GO-SiO₂ and 230 Å for rGO-SiO₂. GO-SiO₂ presents a more regular structure.

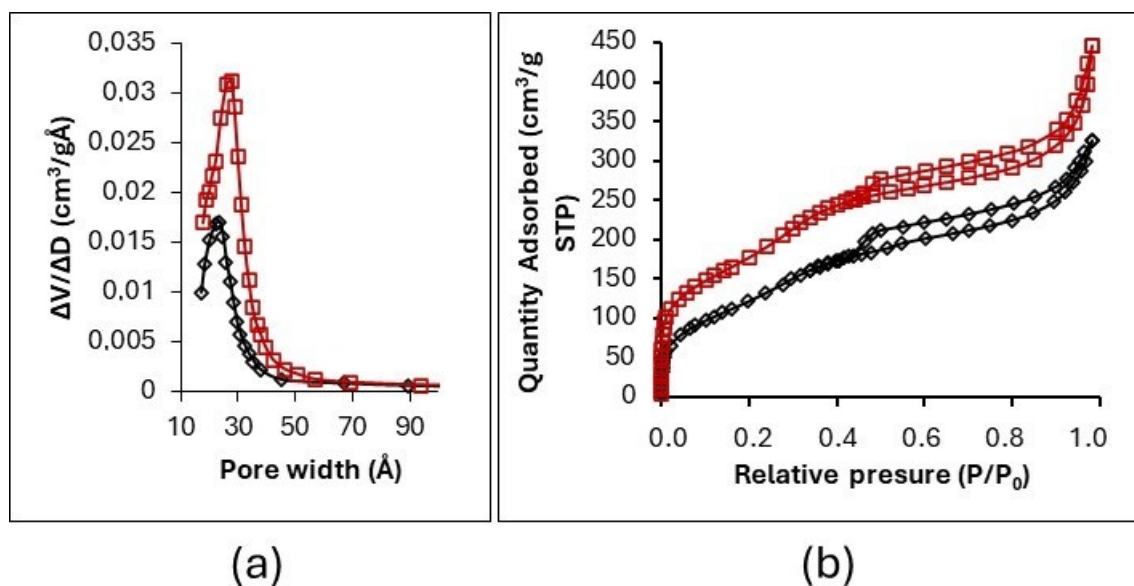


Figure 6. (a) BJH pore-size distributions, showing modes at ~23 Å (GO-SiO₂) and ~27 Å (rGO-SiO₂). (b) N₂ adsorption–desorption isotherms (type IV(a), H3).

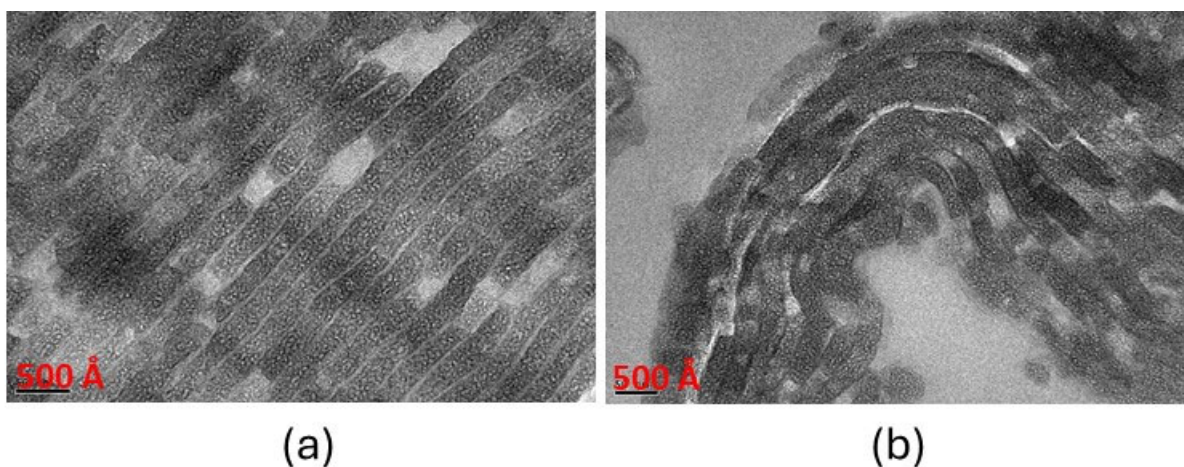


Figure 7. (a) TEM image of the GO-SiO₂ gel; (b) TEM image of the rGO-SiO₂ gel.

Table 2. Textural parameters (S_{BET} , V_{pore} , BJH modal pore diameter, D_{pore}) and SiO₂ content of GO-SiO₂ and rGO-SiO₂.

Sample	S_{BET} (m ² g ^{−1})	V_{pore} (cm ³ g ^{−1})	D_{pore} (Å)	SiO ₂ %
GO-SiO ₂	446	0.46	23	83.6
rGO-SiO ₂	710	0.76	27	87.6

2.2. Characterization of GO-SiO₂-APTMS and rGO-SiO₂-APTMS

Figure 8 compiles the TG-DSC results and MS monitoring at m/z 18 (water) and 44 (CO₂) for the amino-functionalized samples. Both GO-SiO₂-APTMS and rGO-SiO₂-APTMS exhibit an initial mass loss with an endothermic peak at around 90 °C, accompanied by

the release of water and CO₂. Incorporation of APTMS leads not only to desorption of physisorbed ambient water at this temperature (as observed for the non-functionalized samples, Figure 5) but also to the release of chemisorbed ambient CO₂ from the surface.

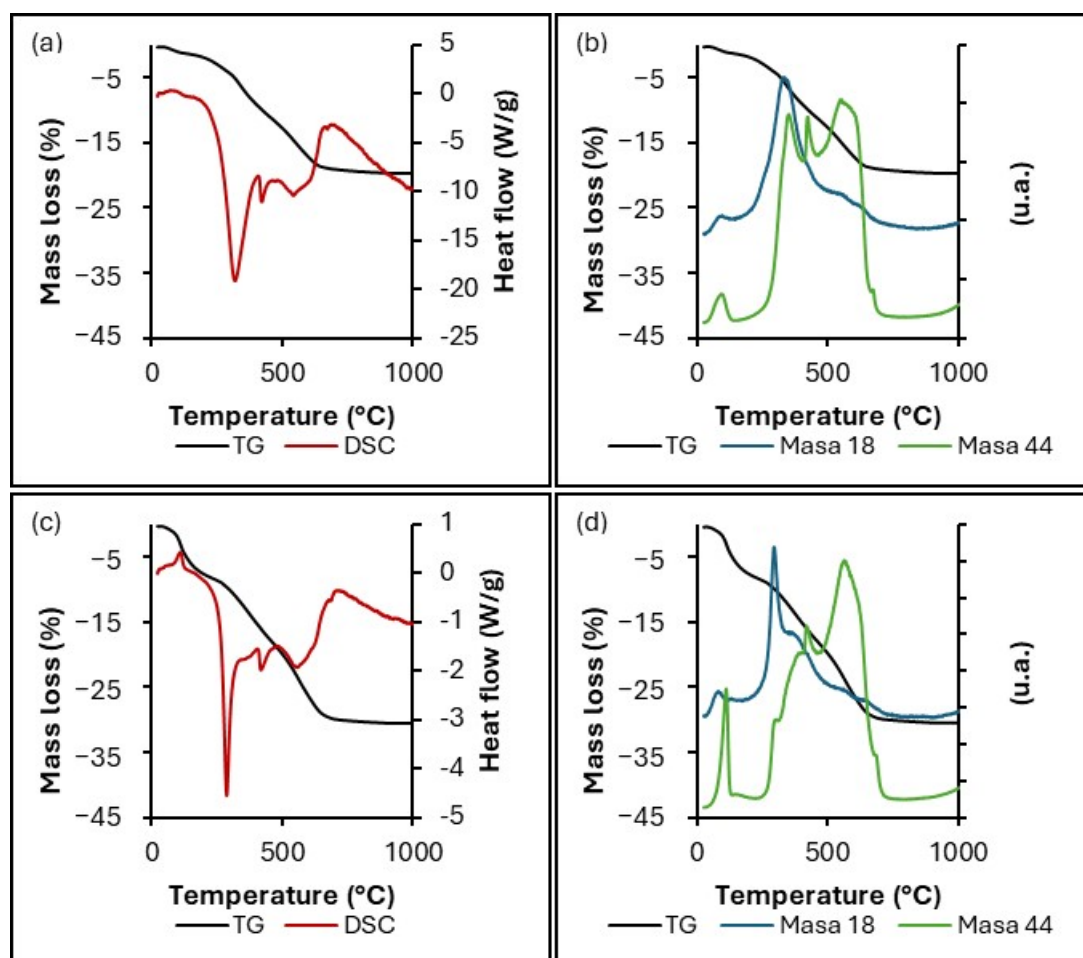


Figure 8. (a,c) TG (black) and DSC (red) curves; (b,d) TG (black) with MS monitoring at m/z 18 (blue) and 44 (green) for GO-SiO₂-APTMS (graphene oxide–silica gel functionalized with APTMS, **top**) and rGO-SiO₂-APTMS (reduced graphene oxide–silica gel functionalized with APTMS, **bottom**).

Subsequent mass losses are associated with exothermic peaks, indicating thermal decomposition. For GO-SiO₂-APTMS, these features arise from the decomposition of oxygen-containing groups on the GO, the decomposition of residual CTAB remaining after ethanol washing, and combustion of the APTMS carbon chain bound to the sample, releasing both water and CO₂. For the rGO-SiO₂-APTMS sample, a similar process occurs; however, only the APTMS carbon chain decomposes in this temperature window.

The final mass loss in both amino-functionalized samples, associated with an endothermic minimum around 520–580 °C, corresponds to the thermal decomposition of the reduced graphene oxide framework (in GO-containing samples, GO is thermally reduced during TG). As indicated by MS monitoring at m/z 18 and 44, CO₂ is predominantly evolved. The white residue corresponds to the silica content, as also observed for the non-functionalized samples.

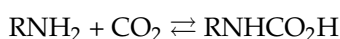
Table 3 reports the mass loss fraction (wt%) assigned to the combustion of the APTMS alkyl chain covalently grafted to the gels, as extracted from the TG profiles in Figure 8. The table also lists the nitrogen content (N, wt%) and the corresponding amine loading (mmol –NH₂ g^{−1}) for both GO-SiO₂-APTMS and rGO-SiO₂-APTMS. The latter values were

obtained by combining the percentage of organic matter removed within the specified temperature interval with the stoichiometric relation between the atomic mass of nitrogen and the molar mass of APTMS (one N per APTMS unit), assuming that the organic mass loss in that interval arises predominantly from the grafted organosilane.

Table 3. Quantification of grafted APTMS in GO-SiO₂-APTMS and rGO-SiO₂-APTMS: TG-derived organic mass loss (wt%), nitrogen content (wt%), and amine loading (mmol −NH₂ g^{−1}).

Sample	TG-Derived Organic Mass Loss (wt%)	Nitrogen Content (wt%)	Amine Loading (mmol −NH ₂ g ^{−1}).
GO-SiO ₂ -APTMS	7.54	1.82	1.30
rGO-SiO ₂ -APTMS	10.33	2.49	1.78

Figure 9 shows the CO₂ adsorption isotherms at 25 °C for GO-SiO₂-APTMS and rGO-SiO₂-APTMS. Both display type I behavior, concave with respect to the x-axis (absolute pressure), with uptake tending to level off at higher pressures, typically associated with monolayer adsorption dominated by chemisorption. In this context, CO₂ reacts with amine groups on the surface to form carbamate species according to the following equilibrium:



This chemisorption mechanism is desirable for carbon capture applications because it implies strong and selective binding of CO₂ at low partial pressures, as encountered in post-combustion gas streams. Type I isotherms also suggest an energetically homogeneous set of adsorption sites, beneficial for predictable performance in practical adsorption systems.

At 25 °C, Table 4 benchmarks the CO₂ uptake at 1.0 atm and 0.1 atm for the two graphene–silica gels alongside a silica-only reference gel (SiO₂-APTMS), synthesized analogously to the present materials but without the graphene component. rGO-SiO₂-APTMS exhibits the highest absolute uptake (41.4 ± 0.4 and 32.3 ± 0.3 cm³ g^{−1} at 1.0 and 0.1 atm, respectively), followed by SiO₂-APTMS (39.8 ± 0.4 and 29.3 ± 0.3 cm³ g^{−1}), whereas GO-SiO₂-APTMS is lower (26.6 ± 0.3 and 17.3 ± 0.2 cm³ g^{−1}). The near-parity between rGO-SiO₂-APTMS and the silica-only reference, despite the former's lower amine loading (Table 3), indicates improved site accessibility within the laminar rGO framework, consistent with the complete removal of CTAB during calcination and the concomitant reduction in steric hindrance across the mesoporous network. When contextualized against state-of-the-art adsorbents, the amine-grafted rGO-SiO₂ gels combine mesoporous accessibility with robust cycling, yielding CO₂ uptakes at 25 °C that are on par with typical amine-functionalized mesoporous silicas under low-pressure conditions while delivering higher per-site utilization (Table 5) and excellent retention after 50 cycles (Table 4, Figure 10). In contrast to predominantly microporous frameworks such as zeolites and many MOFs, the laminar mesopores ($\approx 20\text{--}30$ Å) in our gels facilitate amine accessibility and diffusion, which is directly reflected in the per-site efficiencies reported here.

Accordingly, GO-SiO₂-APTMS shows lower CO₂ uptake (26.6 ± 0.3 and 17.3 ± 0.2 cm³ g^{−1} at 1.0 and 0.1 atm, respectively) and a lower per-site efficiency (59.4%) than rGO-SiO₂-APTMS (41.4 ± 0.4 ; 32.3 ± 0.3 cm³ g^{−1}; 81.0%), and it retains $\approx 90.0\%$ of its initial capacity after 50 cycles versus $\approx 96.3\%$ for rGO-SiO₂-APTMS under the same regeneration protocol.

Using the amine loading reported in Table 3 (mmol −NH₂ g^{−1}), together with the CO₂ uptake reported in Table 4 (converted to a molar basis on the same mass of adsorbent), the per-site chemisorption efficiency can be calculated as

$$\eta = n(\text{CO}_2)/n(-\text{NH}_2) \times 100\%$$

assuming a 1:1 (mol–mol) stoichiometry between CO₂ and the accessible amine groups under the present conditions. As summarized in Table 5, the calculated efficiencies indicate

that rGO-SiO₂-APTMS exhibits a higher CO₂-capture efficiency per amine site than GO-SiO₂-APTMS and SiO₂-APTMS, consistent with the improved textural accessibility inferred from the nitrogen sorption data.

In GO-SiO₂, the exothermic mass loss at ~340 °C with concurrent *m/z* 18 and 44 signals (Figure 5a,b) is assigned to residual CTAB after solvent extraction; consistent with the N₂-sorption data (Figure 6, Table 2), this residual surfactant partially occludes mesopores and limits subsequent amine site accessibility. Taken together, these textural effects rationalize the lower uptake and per-site efficiency of GO-SiO₂-APTMS relative to rGO-SiO₂-APTMS (Tables 4 and 5) and the slightly lower capacity retention during cycling (Figure 10).

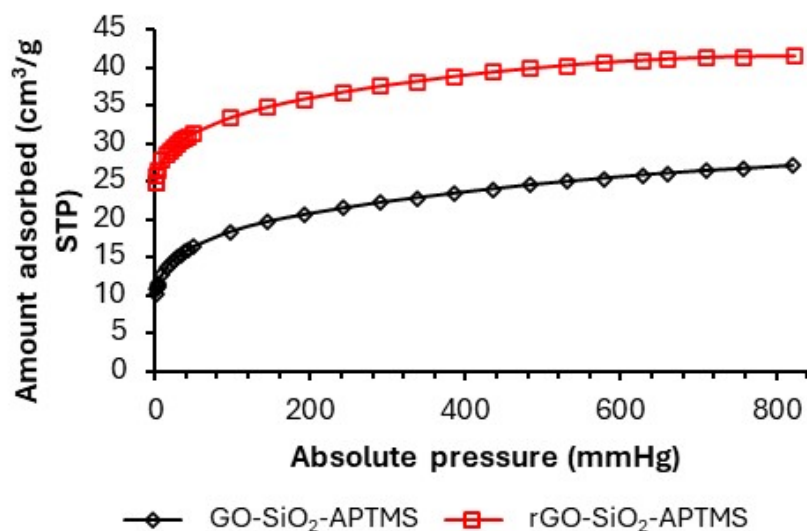


Figure 9. CO₂ adsorption isotherms at 25 °C of GO-SiO₂-APTMS and rGO-SiO₂-APTMS.

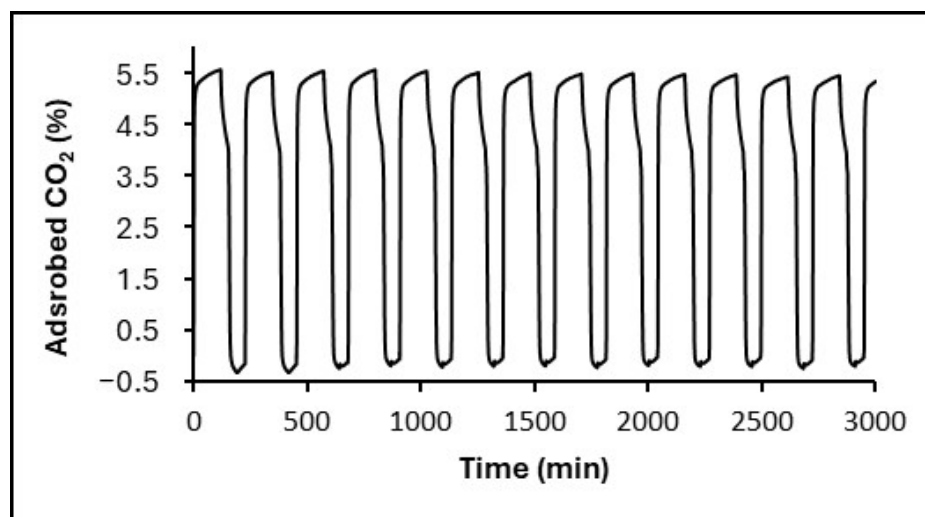


Figure 10. Representative isothermal CO₂ capture-regeneration cycles at 25 °C for rGO-SiO₂-APTMS under a 20% CO₂/N₂ stream (adsorption) and N₂ at 110 °C (regeneration). A rapid initial uptake is followed by a slower approach to equilibrium within each cycle; capacity retention over 50 cycles is reported in Table 6.

Table 4. CO₂ adsorption capacity of GO-SiO₂-APTMS, rGO-SiO₂-APTMS, and SiO₂-APTMS (silica gel functionalized with APTMS) at 1 atm and 0.1 atm, derived from CO₂ adsorption isotherms at 25 °C.

Sample	CO ₂ (1 atm) (cm ³ g ^{−1})	CO ₂ (0.1 atm) (cm ³ g ^{−1})
SiO ₂ -APTMS	39.8 ± 0.4	29.3 ± 0.3
GO-SiO ₂ -APTMS	26.6 ± 0.3	17.3 ± 0.2
rGO-SiO ₂ -APTMS	41.4 ± 0.4	32.3 ± 0.3

Table 5. Efficiency of the chemisorption reaction for carbamate formation.

Sample	Amine Loading (mmol −NH ₂ g ^{−1})	CO ₂ (0.1 atm) (mmol g ^{−1})	% Efficiency (CO ₂ /−NH ₂)
SiO ₂ -APTMS	2.64	1.3	49.2
GO-SiO ₂ -APTMS	1.30	0.77	59.4
rGO-SiO ₂ -APTMS	1.78	1.44	81.0

Table 6. CO₂ captured (mass %, per cycle) during adsorption–desorption cycling at 25 °C in 20% CO₂/N₂, followed by regeneration in N₂ at 110 °C. R₅₀ denotes capacity retention after 50 cycles.

Sample	CO ₂ Mass (%) Cycle 1	CO ₂ Mass (%) Cycle 2	CO ₂ Mass (%) Cycle 3	CO ₂ Mass (%) Cycle 4	CO ₂ Mass (%) Cycle 5	CO ₂ Mass (%) Cycle 6	CO ₂ Mass (%) Cycle 15	CO ₂ Mass (%) Cycle 25	CO ₂ Mass (%) Cycle 50
SiO ₂ -APTMS	4.7	4.5	4.4	4.3	4.2	4.2	4.0	3.8	3.6
GO-SiO ₂ -APTMS	3.0	3.0	3.0	2.9	2.9	2.9	2.8	2.7	2.7
rGO-SiO ₂ -APTMS	5.4	5.3	5.4	5.4	5.3	5.4	5.3	5.2	5.2

2.3. Cyclic Adsorption and Desorption of CO₂

To evaluate stability toward CO₂ capture under repeated operation, we performed cyclic adsorption–desorption tests combining thermogravimetric cycling and extended fixed-bed runs (see Section 4.4). Table 6 compiles the results of the CO₂ adsorption–desorption cycling. In addition to the composites, an amino-functionalized mesoporous silica sample (SiO₂-APTMS), synthesized analogously but without the graphene-based materials, is included. The first notable observation is that rGO-SiO₂-APTMS adsorbs more CO₂ than GO-SiO₂-APTMS, with an increase of 2.4%, consistent with the CO₂ adsorption–desorption isotherms discussed in Figure 9. SiO₂-APTMS shows a CO₂ adsorption capacity similar to that of the samples under study.

For rGO-SiO₂-APTMS and GO-SiO₂-APTMS, the mass percentage of adsorbed CO₂ remains nearly constant up to cycle 15, with a slight decrease in cycles 25 and 50. This translates into retentions of 96.3% and 90.0% for the initial capacity at cycle 50, respectively. In contrast, for GO-SiO₂-APTMS, the adsorbed amount remains stable only during the first three cycles and then progressively decreases. Compared with the sample lacking graphene-based material (SiO₂-APTMS), the adsorption capacity drops even further, down to 76.6%. Therefore, introducing the graphene-based material enhances stability over CO₂ adsorption–desorption cycles, with a more pronounced improvement when the graphene material is in its reduced form.

As an example of the behavior during the first fourteen isothermal CO₂ capture–regeneration cycles at 25 °C, Figure 10 shows the corresponding data for rGO-SiO₂-APTMS. A strong initial CO₂ uptake is observed in the first minutes of each cycle, attributed to chemisorption via carbamate formation between amine groups and the CO₂, followed by a continuous increase over 50 min, approaching equilibrium.

As summarized in Table 6 and illustrated in Figure 10, both amine-functionalized gels show minimal capacity fade. rGO-SiO₂-APTMS retains ≈96.3% of its initial uptake after 50 cycles, whereas GO-SiO₂-APTMS retains ≈90.0%; by contrast, SiO₂-APTMS (without the graphene component) retains ≈76.6%. The superior retention of rGO-SiO₂-APTMS is consistent with its higher accessible surface area and reduced residual surfactant, improving amine site accessibility throughout the laminar mesoporous framework.

2.4. Kinetics and Thermodynamics of CO₂ Capture Reaction

As outlined in Section 2.2, CO₂ uptake proceeds via the CO₂–amine surface reaction, leading to ammonium–carbamate (dry). On this basis, below, we discuss the apparent kinetic order in CO₂ and benchmark its rate constants, as well as the literature values of ΔH and ΔS , to place our 25 °C isotherms of GO-SiO₂-APTMS and rGO-SiO₂-APTMS in context.

In solid-supported primary amines, CO₂ adsorption proceeds predominantly via ammonium–carbamate ion pairs under dry conditions, while bicarbonate–carbonate species become significant in the presence of water [34,35]. This mechanistic picture (zwitterion formation followed by deprotonation by a neighboring amine) is consistently reported across supported-amine systems.

Under the nominally dry conditions used here, CO₂ capture on primary amines proceeds via the classical zwitterion–deprotonation sequence to form an ammonium–carbamate ion pair, whereas in the presence of water, a bicarbonate route can also contribute, effectively requiring only one amine per CO₂. Consistent with this framework, the higher per-site efficiency observed for rGO-SiO₂-APTMS (Table 5) reflects improved site accessibility within the laminar rGO scaffold and general–base assistance by neighboring amines and/or silanols that facilitates the deprotonation step.

At 25 °C, and at low surface coverage, the apparent reaction order in CO₂ is typically close to the first order ($m \approx 0.8$ – 1.0), decreasing toward zero as the surface approaches saturation. Transient uptakes on amine-grafted silica are commonly fitted with pseudo-first-order or Avrami models, which capture the exponential-to-fractal approach to equilibrium; reported apparent rate constants at 25 °C span 10^{-4} – 10^{-2} s^{−1}, depending on amine type/loading, porosity, gas residence time, and humidity [36]. These trends are consistent with an Eley–Rideal-type event [37] between gaseous CO₂ and available surface –NH₂ sites.

Regarding thermodynamics, multi-temperature studies on amine-functionalized silica generally indicate exothermic adsorption, with ΔH_{ads} for primary amines in dry conditions in the -70 to -100 kJ mol^{−1} range (chemisorption), while humid conditions and/or higher coverages often yield apparent heats in the -30 to -60 kJ mol^{−1} range due to changes in speciation and competitive adsorption [38]. The entropy change is negative (≈ -50 to -150 J mol^{−1} K^{−1}), reflecting ordering upon ion pair formation [38]. For GO/rGO-SiO₂ hybrids, the literature indicates that the graphene-derived microenvironment can modulate both kinetics and apparent heats, often improving uptake or mass transfer characteristics relative to bare silica [39].

Because the present work reports single-temperature isotherms at 25 °C, we refrain from extracting system-specific $\Delta H/\Delta S$ values, which require multi-temperature datasets (Van 't Hoff) or microcalorimetry. Instead, we benchmark our materials within the above

literature ranges, which are mechanistically consistent with the shape of our 25 °C isotherms and with the chemistry of APTMS-grafted silica and GO/rGO-SiO₂ composites.

3. Conclusions

Two types of laminar mesoporous gels were formed: GO-SiO₂ and rGO-SiO₂. Both present regular interplanar spacing between GO-based sheets, with mesopore silica filling these spaces; the silica contents are 83.6 and 87.6%, respectively. The nature of the sheets differs because of the surfactant removal method used during synthesis: solvent extraction preserves the GO character, whereas thermal elimination reduces GO to rGO, changing its chemical nature. This change involves the partial elimination of the oxygenated groups on its surface. Calcination eliminates the surfactant completely, unlike solvent extraction, which leaves residual surfactant within the structure. This is reflected in N₂ adsorption-desorption measurements, where textural parameters are higher for rGO-SiO₂.

Amine functionalization of these materials was confirmed by combined TG-DSC analysis and CO₂ adsorption isotherm. The amine-functionalized gels with the highest CO₂ adsorption capacity are those containing reduced graphene oxide (rGO). Moreover, regeneration cycle data indicate that these composites exhibit greater stability of adsorption capacity upon repeated cycling. The CO₂ adsorption isotherms indicate that adsorption occurs predominantly via chemisorption, attributed to the reaction between CO₂ and primary amine sites, which forms carbamates.

Importantly, cyclic tests confirm excellent stability toward CO₂ capture: rGO-SiO₂-APTMS retains ≈96.3% of its initial uptake after 50 cycles, outperforming GO-SiO₂-APTMS (≈90.0%) and SiO₂-APTMS (≈76.6%).

Complete surfactant removal in the rGO-derived gels enhances textural accessibility and translates into higher CO₂ uptake, greater per-site efficiency, and slightly better capacity retention than in the GO-derived gels, where residual CTAB partially occludes mesopores.

In sum, rGO-SiO₂-APTMS couples competitive mesoporous textural metrics for an amine-grafted silica with high per-site efficiency and robust cycling, underscoring its competitiveness relative to conventional silica adsorbents and its practical advantages versus predominantly microporous frameworks.

4. Materials and Methods

4.1. Materials

GO was supplied by Graphenea (San Sebastián, Spain). Cetyltrimethylammonium bromide (CTAB), sodium hydroxide (NaOH, 99%), dodecylamine (98%), tetramethylammonium hydroxide (TMAOH, 98%), tetraethyl orthosilicate (TEOS), fumed silica (98%), and a sodium silicate solution (SiO₂ 26.5–Na₂O 10.6%) were purchased from Sigma Aldrich (St. Louis, MO, USA).

4.2. Synthesis

First, CTAB was intercalated between GO sheets, following the protocol of Wei [3]. Briefly, 2 g of CTAB was dissolved in 40 mL of 0.1 N NaOH. Then, 0.2 g of GO was added, and the mixture was ultrasonicated, followed by stirring for 5 days at room temperature. The resultant suspension was filtered and washed with deionized water. The solid (GO-CTAB) was dried at 60 °C for 3 days.

In a second step, the dried GO-CTAB was stirred in a 1.03% (*w/w*) aqueous dodecylamine solution for 3 h at 50 °C. Then, 8 mL of TEOS was added, and the suspension was stirred for 5 h at 50 °C. The resulting material (GO-CTAB-SiO₂) was centrifuged and dried at 60 °C for 7 days.

Finally, the surfactant template (CTAB) was removed; two different methods were used: thermal treatment and solvent extraction. The thermal treatment consisted of heating GO-CTAB-SiO₂ in air at 10 °C/min up to 380 °C, followed by a 30 min isotherm; the product was labeled rGO-SiO₂. Solvent extraction was carried out with ethanol (80 mL of ethanol per gram of GO-CTAB-SiO₂) at reflux for 3 days; the solid was filtered, washed, and dried at 65 °C. This extraction was performed twice; the sample was labeled GO-SiO₂. Figure 11 shows a diagram summarizing these syntheses.

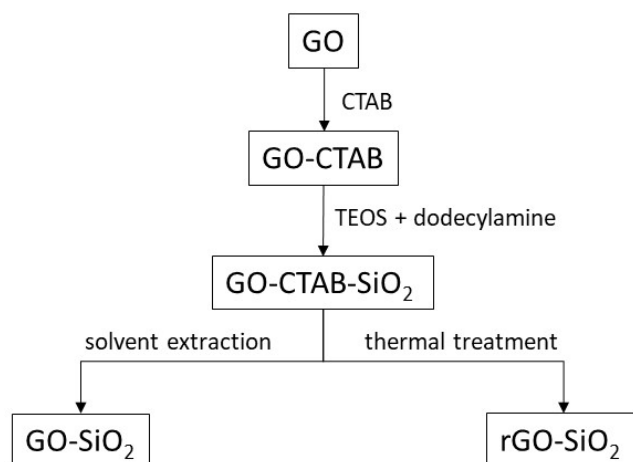


Figure 11. Synthesis diagram of GO-SiO₂ and rGO-SiO₂ gels.

GO-SiO₂ and rGO-SiO₂ gels were functionalized with (3-aminopropyl)trimethoxysilane (APTMS).

In a typical procedure, 0.5 g of the composite was dispersed in 25.0 mL of anhydrous toluene under magnetic stirring. APTMS was added at 5 mmol per gram of gel. The suspension was refluxed under a nitrogen atmosphere for 24 h. The solid product was recovered by vacuum filtration, washed thoroughly with toluene, and dried at 60 °C for 24 h.

The resulting materials were labeled as GO-SiO₂-APTMS and rGO-SiO₂-APTMS.

A mesoporous silica reference functionalized with APTMS (SiO₂-APTMS) was synthesized analogously to the target gels, following the rGO-SiO₂-APTMS protocol but omitting the graphene component.

4.3. Characterization

XRD was performed on a Bruker D8 Advance diffractometer (Billerica, MA, USA) using Cu K α radiation.

XPS was carried out using a SPECS Phoibos 100 MCD5 hemispherical electron analyzer (Berlin, Germany) operated in constant energy mode with a K α Mg X-ray source and an electron flood gun to compensate for sample charging effects. Samples were dried under vacuum prior to analysis.

DSC and TG were performed on a Setaram TG-DSC instrument (Caluire-et-Cuire, France) from room temperature to 1000 °C in air, at a heating rate of 10 °C/min and an air flow of 50 cm³·min^{−1}.

MS was carried out with a ThermoStar GSD 301 T instrument from Pfeiffer Vacuum (Aßlar, Germany) connected in series to the TG-DSC Setaram. The operating pressure ranged from 1·10^{−6} to 5·10^{−6} mbar.

N₂ adsorption–desorption isotherms were recorded on a Micromeritics ASAP-2000 volumetric gas adsorption analyzer at the saturation temperature of nitrogen, over relative pressures of 0 to 1. Prior to measurement, samples were outgassed at 140 °C and 10^{−4} mbar.

for 16 h. Specific surface areas were calculated using the Brunauer–Emmett–Teller (BET) method. Total pore volume (V_{pore}) was taken as the volume of liquid N_2 adsorbed at a relative pressure close to unity ($P/P^0 = 0.95$), calculated according to Gurvitch’s rule. Pore size distributions were obtained using the Barrett–Joyner–Halenda (BJH) method for mesoporous materials [40].

TEM was performed on a JEOL JEM-2100 microscope (Peabody, MA, USA). Samples were prepared using conventional procedures and sectioned into electron-transparent slices by ultramicrotomy.

4.4. CO_2 Capture Evaluation

CO_2 adsorption isotherms were obtained on a Micromeritics ASAP-2000 volumetric analyzer at $25\text{ }^\circ\text{C}$, over relative pressures of 0 to 1. Before measurement, samples were outgassed at $140\text{ }^\circ\text{C}$ and 10^{-4} mbar for 16 h.

TG cycling was used to analyze cyclic CO_2 (adsorbate) adsorption and desorption by the adsorbents developed in this study, using a SETARAM thermobalance. Gas flow rate, temperature, and cycle duration were optimized beforehand. Residual moisture and CO_2 were first removed by purging with nitrogen gas (N_2) at $50\text{ cm}^3\cdot\text{min}^{-1}$ while heating from room temperature to $110\text{ }^\circ\text{C}$ at $10\text{ }^\circ\text{C}\cdot\text{min}^{-1}$. Subsequently, a N_2/CO_2 (4:1, 20% CO_2) stream was introduced into the thermobalance, and the sample mass was monitored for a 5 h period to evaluate CO_2 capture capacity. Desorption was then induced by switching back to pure N_2 and heating to $110\text{ }^\circ\text{C}$ at a rate of $10\text{ }^\circ\text{C}\cdot\text{min}^{-1}$, holding for 1 h, and cooling back to room temperature.

These CO_2 adsorption–desorption cycles were repeated up to six times to assess the stability (Figure 12).

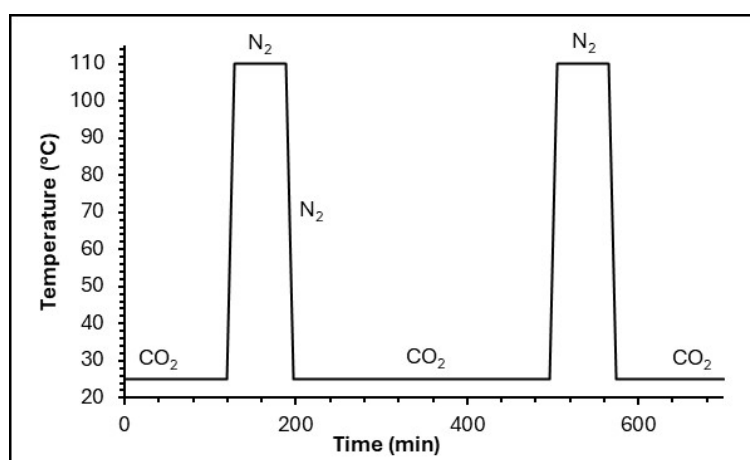


Figure 12. Diagram of the TG cycle process.

For extended cycling (15, 25, or 50 cycles), the samples were first cycled in a fixed-bed microreactor, following the same protocol (exposure to a N_2/CO_2 gas mixture (20% CO_2) for 5 h, followed by regeneration at $110\text{ }^\circ\text{C}$ in N_2 , heating, 1 h isotherm, and cooling), repeated 15, 25, and 50 times.

The samples were then quantitatively analyzed in the thermobalance: an initial N_2 cycle to clean the surface, followed by a full N_2/CO_2 (20%) cycle to determine the CO_2 capture capacity after the fixed-bed cycling.

Author Contributions: Conceptualization, M.G.-B.; methodology, M.G.-B.; validation, C.B. and Á.Y.; formal analysis, M.G.-B.; investigation, M.G.-B.; resources, C.B. and Á.Y.; data curation, M.G.-B.; writing—original draft preparation, M.G.-B.; writing—review and editing, M.G.-B.; visualization,

M.G.-B.; supervision, C.B. and Á.Y.; project administration, C.B.; funding acquisition, C.B. and Á.Y. All authors have read and agreed to the published version of the manuscript.

Funding: This work was supported by the funding of the Margarita Salas Grant for the Training of Young Doctors 2021–2023 of the University of Cantabria.

Institutional Review Board Statement: Not applicable.

Informed Consent Statement: Not applicable.

Data Availability Statement: The data needed to evaluate the conclusions in this paper are present in the manuscript. Additional raw/processed data related to this study may be requested from the author.

Acknowledgments: The authors wish to express their gratitude to the Materials Chemistry Group at the University of Cantabria for their support and for granting access to the scientific equipment.

Conflicts of Interest: The authors declare no conflicts of interest. The funders had no role in the design of the study; in the collection, analyses, or interpretation of the data; in the writing of the manuscript; or in the decision to publish the results.

Abbreviations

The following abbreviations are used in this manuscript:

APTMS	(3-aminopropyl) trimethoxy silane
BET	Brunauer–Emmett–Teller
BJH	Barrett–Joyner–Halenda
CTAB	Cetyltrimethylammonium bromide
Dpt	Department
DSC	Differential scanning calorimetry
GO	Graphene oxide
GO-CTAB	Graphene oxide treated with CTAB
GO-CTAB-SiO ₂	Graphene oxide–silica gel with CTAB
GO-SiO ₂	Graphene oxide–silica gel
GO-SiO ₂ -APTMS	Graphene oxide–silica gel functionalized with APTMS
IUPAC	International Union of Pure and Applied Chemistry
MCM-41	Mobil Composition of Matter No. 41
MOF	Metal–organic framework
MS	Mass spectrometry
QuIPRe	Chemistry and Process and Resources Engineering
rGO	Reduced graphene oxide
rGO-SiO ₂	Reduced graphene oxide–silica gel
rGO-SiO ₂ -APTMS	Reduced graphene oxide–silica gel functionalized with APTMS
SBA-15	Santa Barbara Amorphous-15
SiO ₂ -APTMS	Silica gel functionalized with APTMS
TEM	Transmission electron microscopy
TEOS	Tetraethyl orthosilicate
TG	Thermogravimetry
TMAOH	Tetramethylammonium hydroxide
XPS	X-ray photoelectron spectroscopy
XRD	X-ray diffraction

References

1. Novoselov, K.S.; Geim, A.K.; Morozov, S.V.; Jiang, D.; Zhang, Y.; Dubonos, S.V.; Grigorieva, I.V.; Firsov, A.A. Electric field effect in atomically thin carbon films. *Science* **2004**, *306*, 666–669. [[CrossRef](#)]
2. Singh, V.; Joung, D.; Zhai, L.; Das, S.; Khondaker, S.I.; Seal, S. Graphene based materials: Past, present and future. *Prog. Mater. Sci.* **2011**, *56*, 1178–1271. [[CrossRef](#)]

3. Wei, L.; Lu, W.; Wei, H.; Chen, C.; Hou, Z. Porous sandwich-like silica/graphene nanocomposites obtained via templating of porous silica with CTAB in the gallery region of graphene oxide. *Microporous Mesoporous Mater.* **2017**, *241*, 58–65.
4. Liu, L.; Zou, G.; Yang, B.; Luo, X.; Xu, S. Amine-functionalized mesoporous silica @ reduced graphene sandwichlike structure composites for CO₂ adsorption. *ACS Appl. Nano Mater.* **2018**, *1*, 4695–4702. [[CrossRef](#)]
5. Wang, Z.M.; Wang, W.; Coombs, N.; Soheilnia, N.; Ozin, G.A. Graphene oxide-periodic mesoporous silica sandwich nanocomposites with vertically oriented channels. *ACS Nano* **2010**, *4*, 7437–7450. [[PubMed](#)]
6. Cheng, L.; Qiao, D.; Zhao, P.; He, Y.; Sun, W.; Yu, H.; Jiao, Z. Template-free synthesis of mesoporous succulents-like TiO₂/graphene aerogel composites for lithium-ion batteries. *Electrochim. Acta* **2019**, *300*, 417–425.
7. Chen, P.; Yang, C.; He, Z.; Guo, K. One-pot facile route to fabricate the precursor of sulfonated graphene/N-doped mesoporous carbons composites for supercapacitors. *J. Mater. Sci.* **2019**, *54*, 4180–4191. [[CrossRef](#)]
8. Liou, T.; Lin, M.H. Preparation of mesoporous graphene oxide/SBA-15 hybrid nanoparticles as a potential adsorbent for removal of cationic dyes. *Desalin. Water Treat.* **2019**, *155*, 285–295. [[CrossRef](#)]
9. Vinodh, R.; Babu, C.M.; Abidov, A.; Palanichamy, M.; Tae Jang, H. Facile synthesis of amine modified silica/reduced graphene oxide composite sorbent for CO₂ adsorption. *Mater. Lett.* **2019**, *247*, 44–47. [[CrossRef](#)]
10. Yang, C.; Tong, Y.; Yang, Z.; Xiao, H.; Qi, H.; Chen, F. High-performance aqueous zinc-ion battery based on laser-induced graphene. *Nanomanuf. Metrol.* **2023**, *6*, 16. [[CrossRef](#)]
11. Deng, R.; Ke, B.; Xie, Y.; Cheng, S.; Zhang, C.; Zhang, H.; Lu, B.; Wang, X. All-solid-state thin-film lithium-sulfur batteries. *Nano-Micro Lett.* **2023**, *15*, 73. [[CrossRef](#)]
12. Ding, H.; Wang, J.; Zhou, J.; Wang, C.; Lu, B. Building electrode skins for ultra-stable potassium metal batteries. *Nat. Commun.* **2023**, *14*, 2305. [[CrossRef](#)]
13. Zhang, Z.; Liu, X.; Lu, Y.; Li, H. Exploration of lithium ions storage performance and mechanism of ZrN@reduced graphene oxide composite. *J. Alloys Compd.* **2023**, *959*, 170448. [[CrossRef](#)]
14. Altaf, C.T.; Colak, T.O.; Rostas, A.M.; Mihet, M.; Lazar, M.D.; Iatsunskyi, I.; Coy, E.; Yildirim, I.D.; Misirlioglu, F.B.; Erdem, E.; et al. GO/ZnO-based all-solid-state photo-supercapacitors: Effect of GO:ZnO ratio on composite properties and advice performance. *J. Energy Storage* **2023**, *68*, 107694. [[CrossRef](#)]
15. Chen, X.; Ge, H.; Yang, W.; Liu, J.; Yang, P. Construction of high-performance solid-state asymmetric supercapacitor based on Ti₃C₂T_x MXene/CuS positive electrode and Fe₂O₃@rGO negative electrode. *J. Energy Storage* **2023**, *68*, 107700. [[CrossRef](#)]
16. Fu, X.; Shu, R.Y.; Ma, C.J.; Zhang, Y.Y.; Jiang, H.B.; Yao, M.N. Self-assembled MXene-graphene oxide composite enhanced laser-induced graphene based electrodes towards conformal supercapacitor applications. *Appl. Surf. Sci.* **2023**, *631*, 157549. [[CrossRef](#)]
17. Shanthini, K.; Anitha, C.; Alphonse, N.R.; Velmurugan, K.; Selvam, V. GO-CNT/AgI nanocomposites: A facile synthesis and environmentally friendly method to removal of organic pollutants. *J. Mol. Struct.* **2023**, *1286*, 135500. [[CrossRef](#)]
18. Chen, C.X.; Yang, S.S.; Ding, J.; Ding, L.; Wu, R.; Liu, L.M.; Pang, J.W.; He, L.; Jiang, J.Q.; Ren, N.Q. Existence of chloride ions in high salinity wastewater accelerates the removal of micropollutants over light-driven catalyst. *Appl. Catal. B* **2023**, *334*, 122823. [[CrossRef](#)]
19. Tian, L.; Zhou, P.; Graham, N.; Li, G.; Yu, W. Long-term operation and biofouling of graphene oxide membrane in practical water treatment: Insights from performance and biofilm characteristics. *J. Membr. Sci.* **2023**, *680*, 121761. [[CrossRef](#)]
20. Chen, H.; Guo, Y.; Zhou, K.; Wang, J.; Zeng, Z.; Li, L. Mechanism exploration of surface functional groups and pore size on CO₂ adsorptive separation by GCMC and DFT simulations. *Sep. Purif. Technol.* **2023**, *318*, 123993. [[CrossRef](#)]
21. Zhang, B.; Liu, X.; Wang, H.; Li, K.; Tatsumi, T.; Wang, J. Accessible amino-rich ordered mesoporous silica for carbon dioxide capture. *Mater. Lett.* **2022**, *321*, 132422. [[CrossRef](#)]
22. Kamran, U.; Park, S. Chemically modified carbonaceous adsorbents for enhanced CO₂ capture: A review. *J. Clean. Prod.* **2021**, *290*, 125776. [[CrossRef](#)]
23. González-Barriuso, M.; Pesquera, C.; González, F.; Yedra, A.; Blanco, C. CO₂ capture by amino-functionalized graphene oxide. *Chem. Eng. Trans.* **2019**, *75*, 637–642.
24. González-Barriuso, M.; Gómez, L.; Pesquera, C.; Perdigón, A.C.; González, F.; Yedra, A.; Blanco, C. CO₂ Capture at low temperature by nanoporous silica modified with amine groups. *Chem. Eng. Trans.* **2016**, *47*, 181–186.
25. Hua, Z.L.; Shi, J.L.; Wang, L.; Zhang, W.H. Preparation of mesoporous silica films on a glass slide: Surfactant template removal by solvent extraction. *J. Non-Cryst. Solids* **2001**, *292*, 177–183. [[CrossRef](#)]
26. Marcilla, A.; Beltran, M.; Gómez-Siurana, A.; Martínez, I.; Berenguer, D. Evaluation of the efficiency of solvent extraction for template removal in the synthesis of MCM-41 type materials to be used as tobacco additives for smoke toxicity reduction. *Appl. Catal. A* **2010**, *378*, 107–113. [[CrossRef](#)]
27. Chang, N.; Tang, H.; Bai, L.; Zhang, Y.; Zeng, G. Optimized rapid thermal processing for the template removal of SAPO-34 zeolite membranes. *J. Membr. Sci.* **2018**, *552*, 13–21. [[CrossRef](#)]
28. Hu, M.L.; Masoomi, M.Y.; Morsali, A. Template strategies with MOFs. *Coord. Chem. Rev.* **2019**, *387*, 415–435. [[CrossRef](#)]

29. Al-Gaashani, R.; Najjar, A.; Zakaria, Y.; Mansour, S.; Atieh, M.A. XPS and structural studies of high quality graphene oxide and reduced graphene oxide prepared by different chemical oxidation methods. *Ceram. Int.* **2019**, *45*, 14439–14448. [\[CrossRef\]](#)
30. Cai, J.; Chen, J.; Zeng, P.; Pang, Z.; Kong, X. Molecular Mechanisms of CO₂ Adsorption in Diamine-Cross-Linked Graphene Oxide. *Chem. Mater.* **2019**, *31*, 3729–3735. [\[CrossRef\]](#)
31. Chaus, A.S.; Jiang, X.H.; Pokorný, P.; Piliptsou, D.G.; Rogachev, A.V. Improving the mechanical property of amorphous carbon films by silicon doping. *Diam. Relat. Mater.* **2018**, *82*, 137–142. [\[CrossRef\]](#)
32. Thommes, M.; Kaneko, K.; Neimark, A.V.; Olivier, J.P.; Rodriguez-Reinoso, F.; Rouquerol, J.; Sing, K.S.W. Physisorption of gases, with special reference to the evaluation of surface area and pore size distribution (IUPAC Technical Report). *Pure Appl. Chem.* **2015**, *87*, 10. [\[CrossRef\]](#)
33. Hernando, M.J.; Pesquera, C.; Blanco, C.; González, F. Comparative study of the texture of montmorillonites pillared with aluminum and aluminum/cerium. *Langmuir* **2001**, *17*, 5156. [\[CrossRef\]](#)
34. Said, R.B.; Kolle, J.M.; Essalah, K.; Tangour, B.; Sayari, A. A Unified Approach to CO₂–Amine Reaction Mechanisms. *ACS Omega* **2020**, *5*, 26125–26133. [\[CrossRef\]](#)
35. Li, T.; Yu, Q.; Barzagli, F.; Li, C.; Che, M.; Zhang, Z.; Zhang, R. Energy efficient catalytic CO₂ desorption: Mechanism, technological progress and perspective. *Carbon Capture Sci. Technol.* **2023**, *6*, 100099. [\[CrossRef\]](#)
36. Serna-Guerrero, R.; Sayari, A. Modeling adsorption of CO₂ on amine-functionalized mesoporous silica. 2: Kinetics and breakthrough curves. *J. Chem. Eng.* **2010**, *161*, 182–190. [\[CrossRef\]](#)
37. Weinberg, W.H. Eley–Rideal Surface Chemistry: Direct Reactivity of Gas Phase Atomic Hydrogen with Adsorbed Species. *Acc. Chem. Res.* **1996**, *29*, 479–487. [\[CrossRef\]](#)
38. Wang, J.; Feng, X.; Wen, S.; Zhan, D.; Zhu, X.; Ning, P.; Zhang, Y.; Mei, X. Recent advances in amine-functionalized silica adsorbents for CO₂ capture. *Renew. Sust. Energ.* **2024**, *203*, 114724. [\[CrossRef\]](#)
39. Hack, J.; Maeda, N.; Meier, D.M. Review on CO₂ Capture Using Amine-Functionalized Materials. *ACS Omega* **2022**, *7*, 39520–39530. [\[CrossRef\]](#)
40. Barrett, E.P.; Joyner, L.G.; Halenda, P.P. The determination of pore volume and area distributions in porous substances. I. Computations from nitrogen isotherms. *J. Am. Chem. Soc.* **1951**, *73*, 373–380. [\[CrossRef\]](#)

Disclaimer/Publisher’s Note: The statements, opinions and data contained in all publications are solely those of the individual author(s) and contributor(s) and not of MDPI and/or the editor(s). MDPI and/or the editor(s) disclaim responsibility for any injury to people or property resulting from any ideas, methods, instructions or products referred to in the content.